Soft Matter

PAPER

View Article Online
View Journal | View Issue

Cite this: *Soft Matter*, 2021, **17**, 6326

Measuring colloid–surface interaction forces in parallel using fluorescence centrifuge force microscopy†

Thomas B. LeFevre, [ab] Dimitri A. Bikos, [ab] Connie B. Chang [ab] and James N. Wilking *[ab]

Received 26th March 2021,
Accepted 25th May 2021

DOI: 10.1039/d1sm00461a

rsc.li/soft-matter-journal

Interactions between colloidal-scale structures govern the physical properties of soft and biological materials, and knowledge of the forces associated with these interactions is critical for understanding and controlling these materials. A common approach to quantify colloidal interactions is to measure the interaction forces between colloids and a fixed surface. The centrifuge force microscope (CFM), a miniaturized microscope inside a centrifuge, is capable of performing hundreds of force measurements in parallel over a wide force range (10^{-2} to 10^{4} pN), but CFM instruments are not widely used to measure colloid–surface interaction forces. In addition, current CFM instruments rely on bright-field illumination and are not capable of fluorescence microscopy. Here we present a fluorescence CFM (F-CFM) that combines both fluorescence and brightfield microscopy and demonstrate its use for measuring microscale colloidal-surface interaction forces. The F-CFM operates at speeds up to 5000 RPM, 2.5× faster than those previously reported, yielding a 6.25× greater maximum force than previous instruments. A battery-powered GoPro video camera enables real-time viewing of the microscopy video on a mobile device, and frequency analysis of the audio signal correlates centrifuge rotational speed with the video signal. To demonstrate the capability of the F-CFM, we measure the force required to detach hundreds of electrostatically stabilized colloidal microspheres attached to a charged glass surface as a function of ionic strength and compare the resulting force distributions with an approximated DLVO theory. The F-CFM will enable microscale force measurements to be correlated with fluorescence imaging in soft and biological systems.

I. Introduction

Soft materials are widespread in nature and industry.[1–8] Examples include food,[9,10] personal care products,[11] biomedical supplies,[12] and biological tissues.[13] These materials are characterized by colloidal-scale structures such as drops,[14] particles,[15–17] and polymers,[4,18,19] which range in size from nanometers to micrometers, and the behavior of these structures governs material properties.[2,3,20,21] A defining attribute of soft materials is their mechanical properties, and knowledge of these properties is valuable for both fundamental and applied research. For example, products like toothpaste must be formulated to achieve desired flow properties and the mechanics of tissues and bio-gels play critical roles in diseases like cancer[22,23] and osteoarthritis.[24,25] These properties are governed by interactions between colloidal constituents;[21,26,27] thus, characterizing colloidal interaction forces is important for understanding and controlling soft material mechanical properties.[28,29]

A variety of tools exist for directly measuring colloidal interaction forces, which are both small and wide-ranging, from 10^{-2} to 10^{4} pN.[30–32] With optical trapping, colloids are brought close to one another and the magnitude of the attractive or repulsive forces between them measured as a function of separation distance.[33–35] Tools like atomic force microscopy (AFM)[36,37] measure interactions between colloids and a fixed surface. Both optical trapping and AFM provide high-resolution force information, but measurements are typically performed one at a time, and are not ideal for quantifying heterogeneous systems, which require many measurements to construct statistically significant force distributions. Instead, techniques like magnetic tweezers[32,38] and centrifugal force microscopy (CFM),[39–44] which can perform multiple force measurements in parallel are better suited for characterizing heterogenous systems. CFM is a particularly attractive technique because it is

[a] *Department of Chemical and Biological Engineering, Montana State University, Bozeman, MT, USA. E-mail: jwilking@gmail.com*
[b] *Center for Biofilm Engineering, Montana State University, Bozeman, MT, USA*

† Electronic supplementary information (ESI) available. See DOI: 10.1039/d1sm00461a

capable of multiple simultaneous measurements (*i.e.* force multiplexing) and does not require significant device calibration or user training. A CFM instrument is composed of a miniaturized microscope housed inside a swinging bucket centrifuge. As the centrifuge spins, colloids suspended in liquid and interacting with a coverslip are subjected to an effective gravitational force drawing them away from the surface. By controlling the rotational speed of the centrifuge, well-defined forces can be applied to 100s of individual colloids simultaneously; however, current CFM instruments rely on brightfield optical microscopy to identify and track colloidal objects.[39–44] This illumination technique is adequate for measuring colloidal interaction forces but is limited with regard to spatial resolution and sample characterization. Fluorescence microscopy offers enhanced spatial resolution and access to a wide-variety of sample labelling techniques, but the incorporation of fluorescence imaging into a CFM has not yet been reported. Such an instrument would provide significant benefits for characterizing complex soft and biological materials.

Here we present a fluorescence CFM (F-CFM) capable of performing both fluorescence and brightfield microscopy in combination with microscale force measurements. The F-CFM can perform 100s of interaction force measurements simultaneously. The F-CFM operates at speeds up to 5000 RPM, 2.5× faster than those previously reported, yielding a 6.25× greater maximum force for any given colloid and a resulting force range of 10^{-2} to 10^{5} pN. Additionally, use of a battery-powered GoPro video camera enables real-time transfer of microscopy video to a mobile device during operation, and frequency analysis of the audio signal provided by on-camera microphones correlates centrifuge rotational speed with the video signal. Wireless streaming video allows observation and control of experiments in real time, similar to previous CFM iterations.[43,44] Audio verification of speed, not reported in previous iterations, allows determination of centrifuge speed profiles in standard unmodified benchtop centrifuges that are not controlled through an external computer user interface. We validate the accuracy of the instrument by measuring, at various effective gravities, the time required for fluorescent colloidal microspheres to sediment from one imaging plane to another. To demonstrate the capability of the F-CFM for performing multiple measurements in parallel, we measure the forces required to detach 100s of electrostatically-stabilized colloidal microspheres attached to a charged glass surface as a function of ionic strength and compare the resulting force distributions to a modified Derjaguin–Landau–Verwey–Overbeek (DLVO) theory. The F-CFM will enable microscale force measurements to be correlated with fluorescence markers in soft and biological systems.

II. Methods

A. Instrument

The F-CFM design is based on a brightfield CFM developed for single-molecule force multiplexing.[41] Optical hardware and supporting electronics are housed in a cylindrical 3D-printed clamshell enclosure that splits into two pieces, bisected by a plane parallel to the long axis (Fig. 1A). Supporting electronics include a white brightfield light-emitting diode (LED) (Fig. 1A, i and ii), a blue fluorescent excitation LED (Fig. 1A, iii and iv), and a lithium polymer (LiPo) battery (Fig. 1A, v). For brightfield illumination, a diffuse white LED is soldered to a customized printed circuit board (PCB) along with a 10 kΩ resistor and Japanese solderless terminal (JST) male connector socket (Fig. 1A, right inset). For fluorescent illumination, a blue LED is soldered to another customized PCB along with a 10 Ω resistor and JST male connector socket (Fig. 1A, left inset). A battery can be connected to the brightfield LED, the blue fluorescent LED, or both – resulting in three available illumination modes. When both LEDs are operational, two batteries are used, and a piece of neutral density filter film (ND = 1.2) is placed over the brightfield LED to reduce the reflection of the fluorescence optical beam off the brightfield LED. The F-CFM is operated in any of these modes by connecting the appropriate LiPo battery to the desired LED during instrument assembly. The camera and optical hardware fit into a custom-designed recess within the clamshell housing (Fig. 1B). After the F-CFM module is assembled and battery wiring harness connected, the second clamshell piece closes around the module (Fig. 1C) and the entire module with housing is inserted into the bucket of a commercially available centrifuge (ThermoFisher Sorvall Legend X1R).

During operation, the centrifuge swinging buckets do not fully extend 90° to the rotational axis z during operation, resulting in a non-normal force vector acting on the sample cell. This is illustrated in Fig. 1D. The bucket swings to 76.6° from the rotational axis at 300 RPM and 80.7° from the rotational axisat 1000 to 5000 RPM (see ESI† Note 1 and Fig. S1) The objective tube, containing the sample cell module and objective, connects to a 3D-printed fluorescence cube, containing a 495 nm dichroic mirror and 520 nm bandpass emission filter, which connects to the focusing lens tube to form a tubular microscope which is attached to a camera (Fig. 1E). A 472 nm bandpass excitation filter fits inside the clamshell housing adjascent to the blue LED PCB. The sample cell, constructed from two circular glass coverslips separated by a spacer to create a sealed shallow sample well, is contained in a two-part 3D-printed housing constructed from a sample cell holder and lid that screws into the objective microscope tube (Fig. 1E, inset). Mounting the sample cell on the interior of the objective tube rather than the exterior end of the tube reduces deformation of the sample cell during centrifugation because the thick walls of the objective tube resist deformation better than the thin threads connecting an exterior sample cell holder to the objective tube. This provides less change in focus throughout the experiment, even at 5000 RPM, the highest RPM for which our buckets are rated. A complete exploded-view diagram and parts ordering information are listed in ESI† Fig. S2. CAD files in STEP format for all 3D-printed components are included as ESI† as well.

Recent advances in camera technology enable the F-CFM. Here, we use a compact, wireless GoPro Hero 5 action camera.

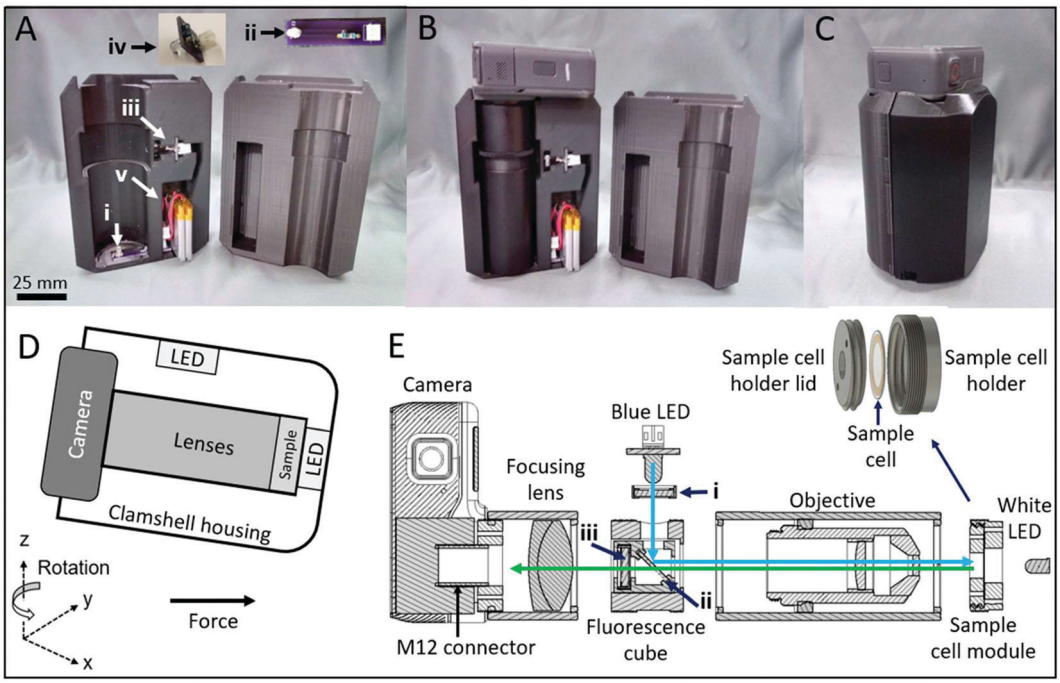

Fig. 1 Fluorescence CFM construction and assembly. (A) Two-part clamshell housing for F-CFM module. Brightfield LED (i and ii), fluorescence LED (iii and iv), and lithium polymer (LiPo) battery (v) are built into the housing. Left inset: Custom printed circuit board (PCB) for fluorescence operation. Right inset: Custom PCB for brightfield operation. (B) The F-CFM module fits inside the clamshell housing during assembly. (C) Clamshell housing closes around F-CFM module. Assembly is ready to be lowered into centrifuge bucket. One of the two camera microphones is visible as a small hole to the left of the power button (square with red circle). (D) Orientation of the F-CFM components, axis of rotation, and centrifugal force vector during operation. (E) Optical components of the F-CFM module. Fluorescence excitation light (blue) travels from the blue LED and through the excitation filter (i) before reflecting off the dichroic mirror (ii) and reaching the sample. Fluorescence emission light (green) travels from the sample, through the dichroic mirror, the emission filter (iii), and the focusing lens, and into the camera sensor. Brightfield illumination light (not shown) follows same path as fluorescence emission light. Inset: Sample cell holder components. Sample cell holder lid screws into sample cell holder, clamping sample cell in place.

The compact form factor of the camera allows more room for fluorescence optical components than previous CFM designs.[39–41] The wireless feature allows the video to be viewed in real time through an application on a smartphone, which also allows the user to start and stop recording remotely. The live video feed is clear up to 4000 RPM and exhibits only minor interference up to 5000 RPM. The GoPro camera has a 6.17 mm × 4.55 mm CMOS 12-megapixel sensor capable of 4k video at 30 frames per second (fps) and 1080p video at 120 fps, stores video on an SD card and requires no electronics knowledge to operate. Here, we use a shorter optical path (≈40 mm) than previous designs (≈90 mm), which require turning mirrors.[39–41] This configuration leads to aberrative vignetting and optical distortion in the corners of the image but offers an acceptable compromise by providing room for important optical components.

B. Fabrication

Construction of F-CFM components is straight-forward and does not require extensive fabrication, programming, or electronics knowledge. The M12 threaded connector that attaches the camera to the focusing tube is made by threading a plain aluminum tube (12 mm O.D. × 10 mm I.D.) using an M12 die along with a die wrench, pipe cutter, and vise. The brightfield LED is soldered to a simple customized PCB (oshpark.com) along with a JST connector and 10 kΩ resistor. The fluorescence LED is soldered to a different customized PCB along with a JST connector and 10 Ω resistor. The brightfield LED requires a strong resistor to prevent oversaturation of the brightfield images, and the fluorescence LED requires a weak resistor to generate enough light to excite the fluorescent dye in the sample. All other components are purchased from optics companies or 3D-printed with a Stanley Model 1 fused deposition modeling (FDM) printer with poly-lactic acid (PLA) 1.75 mm diameter filament. See ESI† Note 2 for assembly information.

C. Experimental protocol

Circular glass coverslips (Thomas Scientific, diameter 18 mm, No. 2 thickness) are cleaned by sonicating for 15 min in each of the following: acetone, isopropanol, 2.0 M NaOH, and pure distilled water, in that order. Prior to the final distilled water sonication step, the coverslips are rinsed several times in pure distilled water to remove excess NaOH. After the final sonication step, the slides are dried with nitrogen. Donut-shaped annular spacers (I.D. = 7 mm, O.D. = 15 mm) are cut from 102.5 μm ± 3.6 μm thickness Kapton tape using a craft cutter (Silhouette CAMEO 2) and adhered to one slide (see ESI† Note 3 and Fig. S3). An annular bead of UV-curing optical adhesive (Norland 61) is deposited inside the annular tape ring on the slide. This bead of adhesive protects the central region of

interest on the slide from being disturbed by air bubbles that form on the edge of the tape during centrifugation, likely due to compression of the tape. After curing the bead of UV adhesive under UV light until hardened (20–300 s depending on the light source), 25 μL of the colloid suspension is pipetted into the shallow well created by the annular spacer and slide. Another cleaned slide is then placed on top of the tape spacer, sealing the sample inside. The inadvertent incorporation of air bubbles must be avoided as their movement during measurements leads to undesired liquid flows.

Once the sample cell is prepared, it is loaded into the sample cell holder which screws into the objective tube. The distance from the sample cell to the objective is adjusted by screwing in the sample cell holder until the interior surface of interest is in focus. This is accomplished by looking at the built-in camera display screen or by attaching the camera to a monitor with the camera mini-USB connection. The sample cell must be illuminated manually, independent of the clamshell holder, during the focusing adjustment before the F-CFM is placed inside the clamshell holder.

After focus is achieved, the F-CFM module is enclosed in the clamshell housing and loaded into a centrifuge bucket. The two sides of the housing are held together by the snug fit within the centrifuge bucket. The weight of the counterbalance at the opposing bucket is verified using an electronic scale, the lid is closed, and the centrifuge is started. When the run is complete, the centrifuge is allowed to come to rest and opened, the camera recording is stopped, and the video files are downloaded to a computer. The onset of centrifuge rotation is distinctly audible in the recorded video, providing a reference point for video image data to be synced with speed data.

The centrifuge used in this study is a swinging bucket ThermoFisher Sorvall Legend X1R with 400 mL buckets (TX-400, p/n 75003655), custom-ordered for PC-control. Operation is controlled by PC instead of the front control pad and records the RPM profile by reporting speed values every 0.5 s. The RPM is measured using a built-in Hall effect sensor and magnets in the rotor base. Detailed speed profiles can be programmed from the included PC control software. A centrifuge without PC control could also be used by manually increasing the centrifuge speed in a stepwise fashion using the centrifuge control pad.

Video files (.mp4) are downloaded from the GoPro SD card onto a PC. Using the FFmpeg toolbox in MATLAB, the.mp4 files are converted into .tiff stacks. Here, for ease of analysis, only one out of every hundred frames is kept for analysis. The frame is cropped from its original 1280 × 720 px to a central 320 × 300 px rectangle in the region of best focus (Fig. 2). These frames are then corrected for drift in Imaris 9.2.1 software. The resulting drift-corrected frames are analyzed one-by-one manually by counting the number of colloids in each frame and recording the colloid counts in a spreadsheet. The frame numbers are synchronized with the reported centrifuge speed to determine the RPM and effective gravity g_{eff} associated with each colloid count. The centrifugal force acting on each microsphere is defined by $F_c = m\omega^2 r$ where r is the moment arm of the centrifuge (0.15 m), ω is the rotational velocity, and m is the effective mass of the colloid. Here, $m = V_c(\rho_c - \rho_f)$, where V_c is the volume of the colloid, ρ_c is the density of the colloid and ρ_f is the density of the fluid.

Independent verification of the reported centrifuge speeds is performed by audio analysis of the .mp4 video files. Using a custom MATLAB R2019b routine, we extract the 48 000 Hz stereo samples recorded on the audio track. The GoPro provides two channels of audio (right and left) which capture similar audio information. Here, we have chosen the left channel for analysis. To match the centrifuge reporting frequency of 0.5 s^{-1}, we fit audio signal clips of 0.5 s duration using a sum-of-sines routine found within the MATLAB Curve Fitting Toolbox. Thus, we can associate each video frame, taken at 25 fps in PAL format, to a corresponding audio clip containing 2000 samples. After fitting the resulting audio waveform using the sum-of-sines fitting routine, frequency information is extracted from the fit parameters, associating an RPM with each 0.5 s time interval. It is convenient to record in PAL rather than NTSC format to ensure an integer number of video fps; this option is available in the "Preferences" menu of the GoPro.

D. Safety considerations

Care must be taken to properly balance the centrifuge. To accomplish this, we set opposing bucket weights to within 1 g of each other. Larger mass imbalances will lead to centrifuge vibration during operation. More importantly, the centers of mass of opposing buckets must match closely as small differences will lead to centrifuge vibration. Given the low cost of a F-CFM module and housing (see ESI† Fig. S2), we counterbalance the F-CFM with a second, identical complete F-CFM module and housing in the opposing bucket. We find this approach is simpler than attempting to replicate the F-CFM module mass distribution with an assembly of similarly weighted objects, and it provides the option of running two different experiments simultaneously.

Care must also be taken to avoid LiPo battery leakage and fire. LiPo batteries should be inspected for damage after each run. If the batteries become dented or smashed, they should be stored in a fireproof LiPo battery bag (*e.g.* Suncentech 180 × 230 mm LiPo Guard battery storage bags) and brought to an electronics retailer for recycling. In initial testing, some of our large batteries (1000 mA h) did leak fluid after extended operation at high speeds; thus, we prefer to use small batteries (40–400 mA h) to reduce the risk of rupture, leakage, and fire. These small batteries provide more than enough current to operate the LED for hours, and we have not observed any damage or leakage due to centrifugation. The centrifuge and buckets are capable of speeds up to 5000 RPM. However, in most cases we prefer to limit our experiments to a maximum speed of 4700 RPM to reduce stress on the camera, batteries, and LEDs.

The F-CFM is housed within a custom-built guarding enclosure composed of an extruded aluminum frame (80/20 brand) and 1/4 in polycarbonate (8020.net) (ESI† Fig. S4). Although our centrifuge was custom-ordered, it contains standard safety features such as thick steel plates surrounding the centrifugation

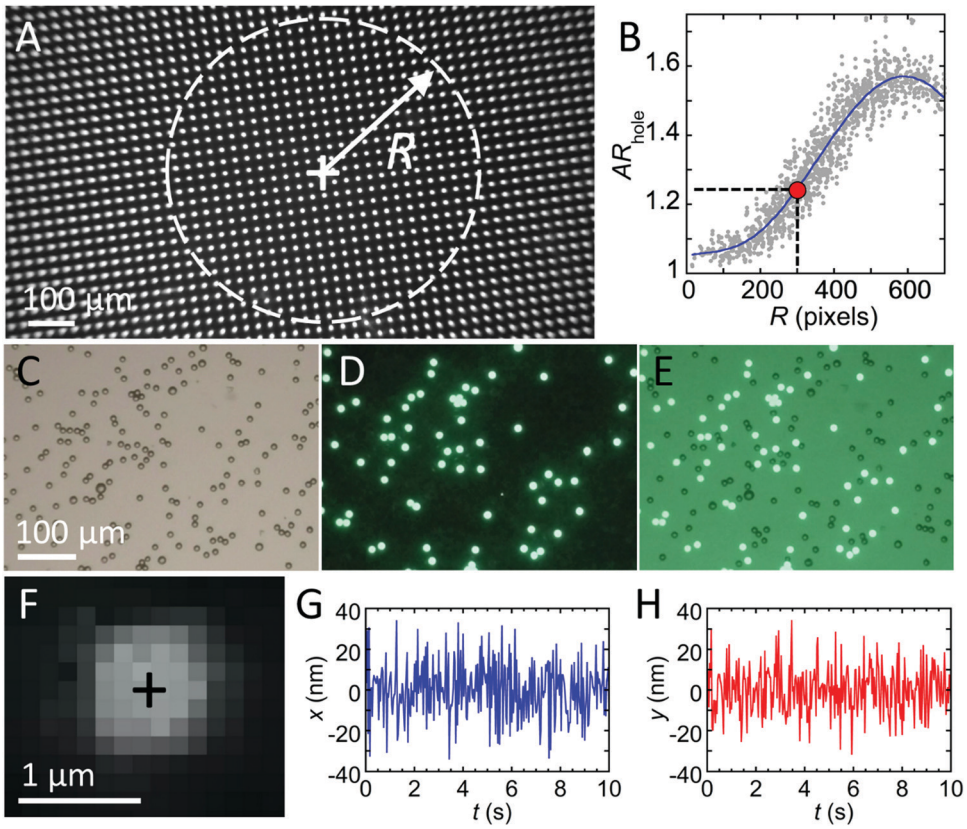

Fig. 2 F-CFM image quality. (A) Brightfield F-CFM image of photomask grid of uniform circular holes (d = 10 μm) reveals optical aberrations near edges. White cross represents center of focus around which white dashes define circle of radius R. (B) Plot of apparent hole aspect ratios AR_{hole} as functions of R for all holes in part A (solid gray circles) fit with a polynomial regression (blue line) to guide the eye (see ESI† Table S1 for fitting form). This can be used to quantify a region of defined image quality. For example, white dashed line in (A) corresponding to R = 300 px encloses holes with $AR_{hole} \leq 1.25$ (red dot). (C–E) F-CFM images (350 × 250 px) of a mixed suspension of green and red fluorescent polystyrene/iron oxide microspheres ($\bar{d}$ = 8.3 μm) captured using (C) brightfield, (D) fluorescence, and (E) concurrent brightfield and fluorescence imaging modes. Red fluorescent microspheres do not fluoresce under these imaging conditions. (F) Digitally zoomed grayscale fluorescence F-CFM image of a small microsphere ($\bar{d}$ = 1.0 μm) fixed by drying to the surface of a glass slide. (G and H) Tracking x and y positions of sphere from part (F) over time t = 10 s using the radial symmetry method.

chamber and an automatic override stop when excess vibration is detected. Since our centrifuge buckets are well-balanced and still within the weight threshold for which the buckets are rated, this polycarbonate guarding is simply meant to help contain debris in the unlikely event of centrifuge failure.

III. Results and discussion

A. Image quality

To assess the image quality provided by the F-CFM using a 20× objective, we image a photomask printed with a grid of uniform circular dots (d = 10 μm) (Fig. 2A). This video frame image measures 1280 × 720 px. The image edges are out-of-focus because we use a short focal length focusing lens. The out-of-focus area is likely due to comatic and spherical aberrations. To quantify the aberration, we measure the aspect ratio (AR) of each dot using ImageJ and plot the aspect ratio as a function of radius R from the center of focus (Fig. 2B). A perfect circle has an aspect ratio of 1, and the aspect ratio increases as aberration increases. The peak of the curve, with an aspect ratio of 1.6, occurs ~575 px from the center of focus. The aspect ratio then dips slightly at the outer edges of the image due to refraction of the light rays that reach the photomask at the highest angle. The center of focus was determined by defining all the dots with AR = 1 and then finding the center of that circle. The center of focus is near, but not directly aligned with the center of the image because the objective, focusing lens, and camera sensor are not perfectly aligned. Fig. 2B provides a measure of aberration across the image, and this information can be used to characterize a region of acceptable image quality. For example, a circle (white dashed line) with R = 300 px enclosing average hole aspect ratios $AR_{hole} \leq 1.25$ is shown in Fig. 2A. Different experiments will require different ranges of acceptable image quality.

To demonstrate the capability of the F-CFM in differentiating two distinct but identically sized colloid populations using fluorescence, we image an aqueous suspension of green and red fluorescent microspheres (Bangs Laboratories; green: $\bar{d}$ = 8.3 ± 0.224 μm (UMDG003) and red: $\bar{d}$ = 8.3 ± 0.28 μm (UMFR003)). The microspheres are nearly identical in size and thus indistinguishable with brightfield imaging alone (Fig. 2C).

The red fluorescent microspheres are not excited by the blue LED illumination, and are effectively non-fluorescent under these imaging conditions; thus, the two microsphere populations are clearly distinguishable when imaged by the F-CFM in fluorescence mode (Fig. 2D and E).

Fluorescence biophysical force measurements (*e.g.* single-molecule) comprise a potentially important application for the F-CFM. Single-molecule force measurements require high-precision, sub-pixel particle tracking within 10s of nm, which can be performed using the F-CFM. To demonstrate, we adhere fluorescently labeled polystyrene colloids ($\bar{d}$ = 1.0 μm, 1 wt%, Thermo Scientific, G0100) to the inner surface of a water-filled sample cell, place the F-CFM module on an optical table to reduce vibrations, and record individual beads for 10 s (Fig. 2F). A radial symmetry particle tracking method records the center of each colloid as a function of time with a maximum resolution of ±0.027 px corresponding to ~2.7 nm. The x (Fig. 2G) and y (Fig. 2H) positions of a single representative bead fluctuates by ±20 nm. This bead tracking resolution is consistent with previous CFM devices. We chose a radial symmetry particle tracking method[45] over alternatives (*e.g.* centroid, Gaussian) for its accuracy, speed, and MATLAB graphical user interface (see ESI† Note 4).

B. Force range

The F-CFM can apply a broad range of forces to colloidal particles. The force range is set by r, ω, and m. Here, our r and minimum ω_{min} are comparable to other commercial centrifuges; thus, the minimum force that can be applied practically is comparable to that reported for other CFMs ($F_{c,min} \approx 10^{-2}$ pN). However, our ω_{max} = 5000 RPM is 2.5× greater than values reported for other CFMs (ω_{max} = 2000 RPM). Since $F_c \propto \omega^2$, this provides a 6.25× increase in the maximum force, compared to other CFMs.[39–41] For a polystyrene microsphere with d = 1 μm and ρ_c = 1.06 g cm^{-3} suspended in water and run at 2000 RPM, the centrifugal force acting on the microsphere $F_{c,max} \approx$ 0.2 pN, while at 5000 RPM, $F_{c,max} \approx$ 1.3 pN. The maximum force can be increased by increasing d or ρ_c, which increases m. For example, from a practical perspective, the largest, most dense colloid would likely be a silica microsphere with $d \approx$ 20 μm and ρ_c = 2.6 g cm^{-3}. At ω_{max} = 5000 RPM, this colloid would experience $F_{c,max} \approx 10^5$ pN. Thus, here we report the force range of the F-CFM to be 10^{-2} to 10^5 pN.

C. Force validation

Most experiments with the F-CFM will subject colloidal suspensions to a well-defined centrifugal force field. While this force is straightforward to calculate from known parameters and should not require calibration, here we offer a simple sedimentation experiment to validate our force predictions. We measure the time required for monodisperse, fluorescently labelled, polystyrene colloidal microspheres ($\bar{d}$ = 4.19 ± 0.27 μm, 0.97 wt%, ρ_c = 1.06 g cm^{-3}, Bangs Laboratories, FSDG006) to sediment from the top of the sample cell to the bottom at different rotational velocities, convert these times to sedimentation velocities, and compare the experimentally measured velocities to theoretical predictions.

With the F-CFM module focused on the colloids at the bottom inside of the sample cell, the F-CFM module is turned upside down to let the microspheres sediment to the inner surface of the coverslip nearest the camera (*i.e.* "top") (Fig. 3A). The total time required for the microspheres to sediment the thickness of the sample cell under gravity g is about 2 min, so the F-CFM module is allowed to sit upside down for 5 min to ensure the microspheres have reached the top of the sample cell before the measurement is started. Then we centrifuge the sample in the F-CFM and measure the time required for the microspheres to sediment to the bottom of the sample cell.

For each measurement, the centrifuge rotation is quickly ramped up to a fixed rotational speed and held at that speed until the colloids reach the inner surface of the coverslip farthest from the camera (*i.e.* "bottom") (Fig. 3B). The centrifuge routine is systematically varied for a range of average rotational speeds, from 150–400 RPM, corresponding to accelerations ranging from 49–216 m s^{-2} and a g_{eff} range of 5–22g. Effective gravity, or relative centrifugal force (RCF), is calculated using $g_{eff} = 11.18r\left(\frac{Q}{1000}\right)^2$ where r is the moment arm of the centrifuge (here, r = 15.0 cm) and Q is the RPM.

The terminal velocity v_t is determined by dividing the settling distance by the measured sedimentation time. The settling distance is set by the thickness of the sample cell h_c which is set by

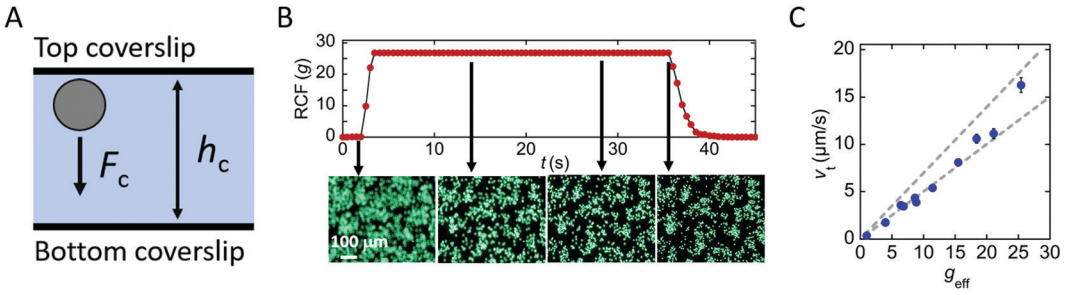

Fig. 3 CFM force validation using colloidal sedimentation. (A) Sample cell cross-section. Gray circle represents microsphere at t = 0 near top coverslip. Not to scale. (B) Plot of relative centrifugal force (RCF) as a function of time t (s) for a representative sedimentation measurement. Sedimentation of green polystyrene fluorescent microspheres ($\bar{d}$ = 4.19 μm) is shown below in representative frames of an optical microscopy movie. (C) Plot of sedimentation terminal velocity v_t (solid blue circles) as a function of effective gravity g_{eff}. Bounding lines represent expected range.

the thickness of the Kapton tape (102.5 ± 3.6 μm). Loading and initiating the centrifuge takes 30 ± 5 s, during which time the colloids sediment 19.7 ± 2.5 μm; so, for our validation, the settling distance under g_{eff} is the modified thickness h_m = 82.8 ± 6.2 μm. Even at the low colloid concentrations used here (<1.0 wt%), many of the microspheres interact with one another hydrodynamically, settle together and arrive at the bottom of the sample cell sooner than those that sediment individually (ESI† Movie 1). Thus, the sedimentation time is defined as the time from the start of the centrifuge rotation to the time at which all the individual microspheres have reached the bottom surface and are fully in focus. A plot of the measured v_t as a function of g_{eff} is shown in Fig. 3C.

To compare these velocity results with expected values, we balance the force due to g_{eff} with the Stokes' drag force on a sphere and solve for the terminal velocity of a sinking sphere: $v_t = \frac{2}{9}\frac{(\rho_c - \rho_f)}{\eta} g_{eff} a^2$. Here, η is the dynamic viscosity of the medium, ρ_c is the density of the colloid, ρ_f is the density of the fluid medium, g_{eff} is the effective gravitational acceleration (RCF), and a is the radius of the colloid (see ESI† Note 5 for more details). For each experiment, we calculate the average g_{eff} over the time frame provided by the observed settling time and plot the predicted v_t as a function of g_{eff}. The predicted v_t plotted as a function of g_{eff} agrees well with our measurements (Fig. 3C). The two gray dashed lines in Fig. 3C indicate the upper and lower predictions for v_t based on uncertainty in h_m, a, and sample temperature (20 °C ≤ T ≤ 23 °C), with the latter dictating the water viscosity (0.9321 cP ≤ η ≤ 1.0016 cP). The measurements fall almost entirely within the two bounds, confirming that we are accurately reporting g_{eff} acting on colloids in the F-CFM. The few points lying below the lower bound can be attributed to potential variations in tape thickness (*i.e.* sedimentation distance) and colloid density, and the fact that we wait for all colloids to reach the lower surface, thus effectively excluding from our measurements the fastest settling colloids, which are likely interacting hydrodynamically.

D. Centrifuge rotational frequency from audio signal analysis

Instantaneous rotational frequencies, reported as centrifuge RPM, may be independently validated by analysis of the audio signal recorded by the GoPro microphone during F-CFM operation (Fig. 4). Audio sample waveforms are a record of the sounds produced by the physical motion of the rotor, effectively

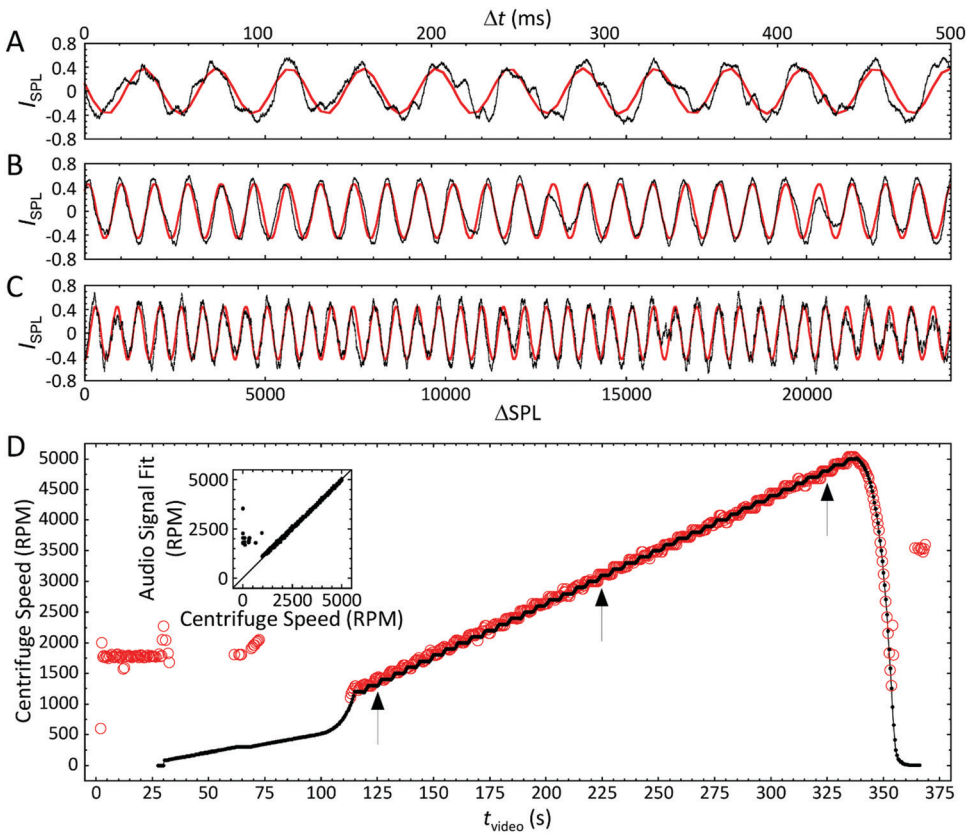

Fig. 4 Audio waveforms reveal centrifuge speed. (A–C) Sections of 48 000 Hz audio samples (black traces) recorded during the beginning, middle, and end of a linearly accelerating F-CFM run. Audio sample (SPL) traces as functions of increments of time (Δt, upper x-axis) and sample number (ΔSPL, lower x-axis) are fit using equation, $I_{SPL} = A\sin(ft + \varphi)$ (solid red lines) where I_{SPL} represents recorded sample intensity (arbitrary units), A amplitude, f frequency (rad), t time (s), and φ offset. Fit parameter f is used to calculate centrifuge speed values of (A) 1429, (B) 3114, and (C) 4800 RPM operation. (D) Centrifuge speed (RPM) reported by instrument (solid black circles, solid black line guides the eye) plotted alongside audio-calculated RPM (open red circles) fit to intervals of 0.5 s (24 000 samples at 48 000 Hz). Arrows indicate locations of parts A–C. Inset: Centrifuge speed values (RPM) from both audio signal fits and magnetic encoder at corresponding times show excellent agreement when RPM > 1000.

providing a sinusoidal signal wherein rotational frequency information is encoded. To illustrate this, we record an audio-visual movie of a linear ramp of centrifuge speed from 0 to 5000 RPM during which audio is recorded at a sampling rate of 48 kHz. For the case of a F-CFM movie taken at 25 fps, each image frame represents a duration of 0.04 s. To compare the data obtained using audio signals with the data reported by the centrifuge magnetic encoder, we divide the audio samples into 0.5 s intervals, each corresponding to 24 kHz samples (Fig. 4A–C, black traces). Using a customized MATLAB routine (see Experimental protocol), we fit these samples to a sinusoidal function, where I is the recorded sample intensity (arbitrary units), A is the amplitude, f is the frequency in rad s^{-1}, t is time, and φ is the offset (Fig. 4A–C, red fits) which tracks the waveforms. Every 0.5 s interval in the movie is given a sine fit, and fitting parameter frequency f is used to determine the RPM value (Fig. 4D). At centrifuge speeds <1000 RPM, cumulative acoustic effects mask the waveform frequency information, but for values >1000 RPM, any harmonic effects are minimized, and values track with those reported by the on-board magnetic encoder (Fig. 4D, inset). Individual measurements in this range routinely differ by $<3.0\%$ from the magnetically encoded values.

E. Colloid detachment force measurements

To demonstrate the capability of the F-CFM for performing multiple force measurements in parallel, we induce attractive interactions between electrostatically stabilized colloids with a negative net surface charge and a negatively charged glass coverslip and measure the forces required to remove these colloids from the coverslip. We explore a range of attractive forces by suspending monodisperse polystyrene/iron oxide microbeads (Sigma-Aldrich, 49664, 5.0 wt%, $\bar{d} = 10.41 \pm 0.13$ μm, $\rho_c = 1.71$ g cm^{-3}) in 0.25× (ionic strength $I = 0.053$ M) phosphate buffered saline (PBS) solution and varying the concentration of NaCl (0.1 M, 0.5 M, 1.25 M, and 2.5 M). The interactions between a charged microsphere and like-charged wall are described by DLVO theory as the sum of a van der Waals attraction and an electrostatic repulsion. The addition of salt to the colloidal suspension screens the electrostatic repulsion, thus increasing the relative contribution of the van der Waals attraction. PBS is added to buffer the pH to mitigate changes in surface charge with changes in ionic strength.[46] For experiments with 0.25× PBS, the pH decreases from 7.6 to 6.6 as the concentration of added NaCl increases from 0.1 M to 2.5 M.

For each measurement, the suspension is loaded into the sample cell, and the colloids are settled and adhered to the interior glass surface of the coverslip. The cell is then oriented such that the g_{eff} acts to draw the colloids away from the surface, and the centrifuge rotational speed is ramped up at 8.9 RPM s^{-1} from 0–4700 RPM, corresponding to 1–283 RCF. Colloids detach with increasing rotational speed (Fig. 5A and ESI† Movie 2, Movie 3). Colloid detachment between sequential frames is determined using a manual image analysis process (Fig. 5B and ESI† Note 6). Detachment counts are normalized to the initial number of attached colloids to determine the fraction of colloids detached f_d, averaged across three runs per condition with 100–189 colloids tracked per run, and plotted as a function of F_c (Fig. 5C). We observe that most colloids detach within the range of applied forces. In addition, the force required to detach colloids increases with increasing ionic strength. To better visualize the dependence of colloid attachment strength as a function of ionic strength, we plot bead-detachment events for each of the four different conditions as probability distributions (Fig. 5F). We find that the data are fit well by a log-normal probability distribution (see ESI† Table S3), with the mode of the distribution increasing with increasing ionic strength.

To calculate the expected strength of the colloidal interaction with the glass surface, we use a modified DLVO model.[47] Colloidal interactions are commonly characterized by an interaction potential where the interaction energy U is plotted as a function of the gap between the two surfaces h; here, instead, for comparison with our experimental force measurements, we calculate and plot the total interaction force F_I as a function of h. For our system, the modified DLVO model predicts two minima: a deep primary minimum at small separation distances ($h < 0.5$ nm) and a shallower secondary minimum at intermediate distances ($h \approx 2$ nm). A representative $F_I(h)$ curve for one solution condition (0.5 M NaCl + 0.25× PBS) is shown in Fig. 5D (see ESI† Note 7 for DLVO equations and assumptions). During loading, as the microspheres are drawn to the glass surface by gravity, they will be drawn into the secondary minimum; however, they are unlikely to overcome the barrier to enter the primary minimum. Thus, we assume the force F_d, required to remove the colloids from the surface of the glass at a separation distance h is equal to the depth of the secondary minimum (Fig. 5D, dashed lines and inset).

To compare our results with expected values, we co-plot the force values associated with the mode of each distribution from Fig. 5F as a function of ionic strength (Fig. 5E, solid blue circles) together with predictions from the modified DLVO model (Fig. 5E, gray dashed lines). To represent the uncertainty in surface charge potential[48] of the glass surface ψ_g and colloid surface ψ_{cs} (see ESI† Note 7) we include two limiting cases as bounding lines: a high surface charge case ($\psi_g = 300$ mV, $\psi_{cs} = 100$ mV) represented by the lower gray dashed line in Fig. 5E, and a low surface charge case ($\psi_g = 150$ mV, $\psi_{cs} = 30$ mV) represented by the upper gray dashed line in Fig. 5E. We find good agreement between experimental and expected detachment force values at low ionic strength, but deviation at higher ionic strengths, where the calculated detachment forces F_d are greater than observed values. These differences could be attributed to surface charge uncertainty,[49–56] spatial heterogeneities of the glass substrate surface potential,[57–60] and surface roughness.[31,37,61–65] Despite the disagreement at high ionic strength, our results reflect the capability of the F-CFM to perform 10s to 100s of force measurements in parallel.

The F-CFM could be used to perform a variety of other parallel force measurements including measurement of other colloidal interaction potentials (*e.g.* depletion and steric), single molecule forces,[39–41] microbial adhesion[41,66] and emulsion

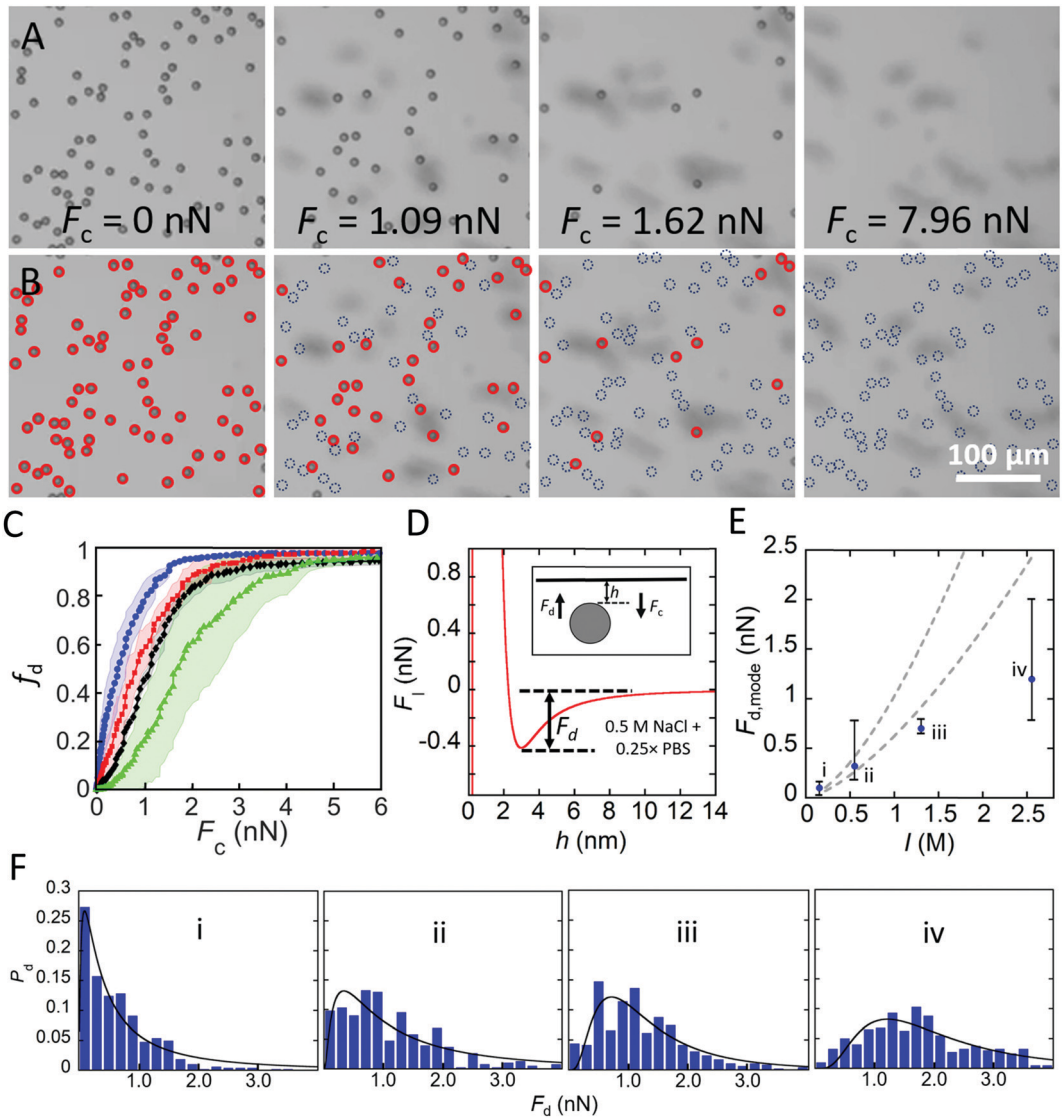

Fig. 5 Colloid detachment force distributions as functions of electrolyte concentrations. (A) Representative optical microscopy images (cropped for better visualization) recorded by the F-CFM show electrostatically stabilized polystyrene/iron oxide colloidal microspheres ($\bar{d}$ = 10.4 µm) being detached from a glass coverslip surface during a force ramp from 1–283 relative centrifugal force (RCF). Images are cropped to represent the area of best focus. (B) Images from (A) indicating attached, in-focus bead locations (solid open red circles) and former locations (dashed open blue circles) of now detached, out-of-focus beads. Scale bar = 100 µm (A and B) (C) Fractions of total colloids detached f_d as a function of applied centrifugal force F_c for NaCl concentrations 0.1 M (solid blue circles), 0.5 M (solid red squares), 1.25 M (solid black diamonds), and 2.5 M (solid green triangles). Solid lines represent the averages of three runs and transparent envelopes indicate one standard deviation. (D) Estimated interaction force F_I as function of gap distance h calculated using DLVO theory predicts a detachment force F_d = 0.040 nN for 0.5 M NaCl + 0.25× PBS. Chosen y-axis range does not allow the depth of primary minimum or height of energy barrier to be seen. Inset: Schematic of a bead at distance h from glass slide surface subjected to centrifugal force F_c and detachment force F_d. (E) Mode of the detachment force $F_{d,mode}$ (solid blue circles) from the distribution peaks in (F) as a function of ionic strength I. Bounding lines represent expected range (see ESI† Note 6 for parameter assumptions and ESI† Table S3 for upper and lower fit parameters). (F) Normalized probability distributions of detachment forces for each experimental condition (i) 0.1 M, (ii) 0.5 M, (iii) 1.25 M, and (iv) 2.5 M, each with 0.25× PBS. Solid lines represent fits to log-normal distribution function (ESI† Table S2).

stability under compression in real time. Future iterations of the F-CFM design could benefit from additional modifications. For example, a second camera sensor could be added below the sample cell to allow transmitted light imaging separately and concurrently with fluorescence imaging. This would improve the image quality for both the transmitted and fluorescence image compared to the current combined "two-in-one" fluorescence and brightfield image. A motorized sample holder that can move in the z-axis could be incorporated for precise real-time mechanical image focusing. Currently, the sample is focused manually at the start of the experiment and cannot be adjusted during the experiment. The ability to move the sample in the z-axis while the centrifuge is spinning would allow focusing on samples as they change position in the sample cell. Real-time focusing could also prevent the reduction in clarity caused by flexing of the sample cell out of the focal plane inherent

in high-speed experiments. A second fluorescence cube could be integrated to allow for multiple fluorophores to be imaged in a single run. This would require additional miniaturization of some components or a larger swinging bucket. Mirrors could be added to directly image the bottom of the surface of interest, allowing non-transparent substrates to be characterized. Other mirror configurations could also allow the sample to be imaged from the side in order to track colloid motion after detachment, although this would limit the number of in-focus colloids. Further miniaturization and ruggedization would also allow the F-CFM to be incorporated into a fixed rotor ultracentrifuge, enabling detachment force measurements on colloids such as bacteria and viruses. Fluidic pumps could also be integrated into the empty remaining centrifuge buckets to alter solution conditions during centrifugation, for example, enabling the concentration of electrolytes in the suspension to be tuned until the point of colloid detachment. Biological samples could be characterized by functionalizing the glass cover slips with silanes followed by ligands of interest. Alternatively, a different transparent material such as PMMA or polypropylene could be used in place of cover slips if the functionalization is better suited to that material.

IV. Conclusion

To our knowledge, the F-CFM is the first CFM to incorporate fluorescence microscopy. Additionally, the F-CFM is the first CFM used for colloid interaction force measurements and the first CFM to operate up to 5000 RPM. This F-CFM is easy to assemble, requiring only basic knowledge of electronics and fabrication. Additionally, the audio microphone provides highly accurate rotational speed information for CFM configurations that lack a centrifuge with a computer interface or on-board magnetic encoder. The wireless F-CFM provides high resolution video with acceptable levels of aberrative vignetting to perform nm-scale, sub-pixel particle tracking. Three illumination modes are available: brightfield, fluorescence, and combined brightfield and fluorescence. Using the F-CFM, we induce attractive interactions between 100s of colloids and a glass coverslip, measure their adhesion force as a function of ionic strength, and show excellent correspondence with prediction at low ionic strength using a modified DLVO model.

Funding

This work was supported by the National Science Foundation (DMR-1455247, DMR-1753352, and OIA-1736255).

Conflicts of interest

There are no conflicts of interest to declare.

Acknowledgements

Special thanks to Wesley Wong and Darren Yang for generously showing us their CFM and explaining its construction and operation. We also thank Matthew Griffin and Mandy Rutherford from the Montana State University Makerspace for their help in the early design stages of this project, and Aaron D. Benjamin for useful discussions.

References

1 M. Daoud, S. N. Lyle and C. E. Williams, *Soft Matter Physics*, Springer, Berlin Heidelberg, 2013.
2 P. M. Chaikin and T. C. Lubensky, *Principles of Condensed Matter Physics*, Cambridge University Press, 2000.
3 W. B. Russel, W. B. Russel, D. A. Saville and W. R. Schowalter, *Colloidal Dispersions*, Cambridge University Press, 1991.
4 M. Rubinstein and R. H. Colby, *Polymer Physics*, OUP, Oxford, 2003.
5 T. Farjami and A. Madadlou, *Trends Food Sci. Technol.*, 2019, **86**, 85–94.
6 T. Kokubo, H. M. Kim and M. Kawashita, *Biomaterials*, 2003, **24**, 2161–2175.
7 M. C. Marchetti, J. F. Joanny, S. Ramaswamy, T. B. Liverpool, J. Prost, M. Rao and R. A. Simha, *Rev. Mod. Phys.*, 2013, **85**, 47.
8 M. M. Fryd and T. G. Mason, in *Annual Review of Physical Chemistry*, ed. M. A. Johnson and T. J. Martinez, Annual Reviews, Palo Alto, 2012, vol. 63, pp. 493–518.
9 R. Mezzenga, P. Schurtenberger, A. Burbidge and M. Michel, *Nat. Mater.*, 2005, **4**, 729–740.
10 A. Donald, *Nat. Mater.*, 2004, **3**, 579–581.
11 R. Brummer, *Rheology Essentials of Cosmetic and Food Emulsions*, Springer, Berlin Heidelberg, 2006.
12 N. A. Peppas, *Hydrogels in Medicine and Pharmacy: Fundamentals*, CRC Press, 2019.
13 Y. C. Fung, *Biomechanics: Mechanical Properties of Living Tissues*, Springer, New York, 2013.
14 T. G. Mason, *Curr. Opin. Colloid Interface Sci.*, 1999, **4**, 231–238.
15 P. J. Lu and D. A. Weitz, *Ann. Rev. Condens. Matter Phys.*, 2013, **4**, 217–233.
16 D. Vlassopoulos and M. Cloitre, *Curr. Opin. Colloid Interface Sci.*, 2014, **19**, 561–574.
17 Z. Adamczyk and P. Warszynski, *Adv. Colloid Interface Sci.*, 1996, **63**, 41–149.
18 J. N. Wilking, T. E. Angelini, A. Seminara, M. P. Brenner and D. A. Weitz, *MRS Bull.*, 2011, **36**, 385–391.
19 A. D. Benjamin, R. Abbasi, M. Owens, R. J. Olsen, D. J. Walsh, T. B. LeFevre and J. N. Wilking, *Biomed. Phys. Eng. Express*, 2019, **5**, 1–10.
20 R. G. Larson, *The Structure and Rheology of Complex Fluids*, OUP, USA, 1999.
21 T. G. Mason and D. A. Weitz, *Phys. Rev. Lett.*, 1995, **75**, 2770–2773.
22 G. Lee, S.-B. Han, J.-H. Lee, H.-W. Kim and D.-H. Kim, *ACS Biomater. Sci. Eng.*, 2019, **5**, 3735–3752.
23 S. Verbruggen, *Mechanobiology in Health and Disease*, Elsevier Science, 2018.

24 J. C. Erhart-Hledik, E. F. Chehab, J. L. Asay, J. Favre, C. R. Chu and T. P. Andriacchi, *Osteoarthritis Cartilage*, 2021, **29**(5), 687–696.
25 D. L. Zignego, J. K. Hilmer and R. K. June, *J. Biomech.*, 2015, **48**, 4253–4261.
26 T. G. Mason, J. Bibette and D. A. Weitz, *Phys. Rev. Lett.*, 1995, **75**, 2051–2054.
27 P. Menut, S. Seiffert, J. Sprakel and D. A. Weitz, *Soft Matter*, 2012, **8**, 156–164.
28 F. L. Leite, C. C. Bueno, A. L. Da Roz, E. C. Ziemath and O. N. Oliveira, *Int. J. Mol. Sci.*, 2012, **13**, 12773–12856.
29 M. A. Meyers, P. Y. Chen, A. Y. M. Lin and Y. Seki, *Prog. Mater. Sci.*, 2008, **53**, 1–206.
30 Y. Liang, N. Hilal, P. Langston and V. Starov, *Adv. Colloid Interface Sci.*, 2007, **134-135**, 151–166.
31 G. Trefalt, T. Palberg and M. Borkovec, *Curr. Opin. Colloid Interface Sci.*, 2017, **27**, 9–17.
32 C. Gosse and V. Croquette, *Biophys. J.*, 2002, **82**, 3314–3329.
33 L. Wilson, P. T. Matsudaira and M. P. Sheetz, *Laser Tweezers in Cell Biology*, Elsevier Science, 1997.
34 D. G. Grier, *Curr. Opin. Colloid Interface Sci.*, 1997, **2**, 264–270.
35 K. Kegler, M. Salomo and F. Kremer, *Phys. Rev. Lett.*, 2007, **98**, 058304.
36 H. J. Butt, R. Berger, E. Bonaccurso, Y. Chen and J. Wang, *Adv. Colloid Interface Sci.*, 2007, **133**, 91–104.
37 H. J. Butt, B. Cappella and M. Kappl, *Surf. Sci. Rep.*, 2005, **59**, 1–152.
38 M. M. van Oene, L. E. Dickinson, B. Cross, F. Pedaci, J. Lipfert and N. H. Dekker, *Sci. Rep.*, 2017, **7**, 1–11.
39 K. Halvorsen and W. P. Wong, *Biophys. J.*, 2010, **98**, L53–L55.
40 T. Hoang, D. S. Patel and K. Halvorsen, *Rev. Sci. Instrum.*, 2016, **87**, 1–5.
41 D. Yang, A. Ward, K. Halvorsen and W. P. Wong, *Nat. Commun.*, 2016, **7**, 1–7.
42 L. Kou, L. Jin, H. Lei, C. Hu, H. Li and X. Hu, *J. Microsc.*, 2019, **273**, 178–188.
43 J. A. Punnoose, A. Hayden, L. F. Zhou and K. Halvorsen, *Biophys. J.*, 2020, **119**, 2231–2239.
44 M. W. H. Kirkness and N. R. Forde, *Biophys. J.*, 2018, **114**, 570–576.
45 R. Parthasarathy, *Nat. Methods*, 2012, **9**, 724–726.
46 S. H. Behrens and D. G. Grier, *J. Chem. Phys.*, 2001, **115**, 6716–6721.
47 J. Gregory, *J. Colloid Interface Sci.*, 1974, **51**, 44–51.
48 M. Elimelech, J. Gregory, X. Jia and R. Williams, *Particle Deposition and Aggregation*, Butterworth-Heinemann Ltd, 1995.
49 R. Folkersma, A. J. G. van Diemen and H. N. Stein, *Langmuir*, 1998, **14**, 5973–5976.
50 K. M. Ohsawa, M. Murata and H. Ohshima, *Colloid Polym. Sci.*, 1986, **264**, 1005–1009.
51 A. Garg, C. A. Cartier, K. J. M. Bishop and D. Velegol, *Langmuir*, 2016, **32**, 11837–11844.
52 Z. Adamczyk, A. Bratek-Skicki, P. Dabrowska and M. Nattich-Rak, *Langmuir*, 2012, **28**, 474–485.
53 E. C. Y. Yan, Y. Liu and K. B. Eisenthal, *J. Phys. Chem. B*, 1998, **102**, 6331–6336.
54 O. El-Gholabzouri, M. A. Cabrerizo and R. Hidalgo-Alvarez, *J. Colloid Interface Sci.*, 1999, **214**, 243–250.
55 Y. Tabata and Y. Ikada, *Biomaterials*, 1988, **9**, 356–362.
56 W. M. Brouwer and R. L. J. Zsom, *Colloids Surf.*, 1987, **24**, 195–208.
57 Y. Luthi, J. Ricka and M. Borkovec, *J. Colloid Interface Sci.*, 1998, **206**, 314–321.
58 A. M. Schrader, J. I. Monroe, R. Sheil, H. A. Dobbs, T. J. Keller, Y. X. Li, S. Jain, M. S. Shell, J. N. Israelachvili and S. G. Han, *Proc. Natl. Acad. Sci. U. S. A.*, 2018, **115**, 2890–2895.
59 J. J. Cras, C. A. Rowe-Taitt, D. A. Nivens and F. S. Ligler, *Biosens. Bioelectron.*, 1999, **14**, 683–688.
60 P. Warszynski and Z. Adamczyk, *J. Colloid Interface Sci.*, 1996, **1878**, 283–295.
61 R. M. Pashley, P. M. McGuiggan, B. W. Ninham and D. F. Evans, *Science*, 1985, **229**, 1088–1089.
62 Y. I. Rabinovich, J. J. Adler, A. Ata, R. K. Singh and B. M. Moudgil, *J. Colloid Interface Sci.*, 2000, **232**, 10–16.
63 Y. I. Rabinovich, J. J. Adler, A. Ata, R. K. Singh and B. M. Moudgil, *J. Colloid Interface Sci.*, 2000, **232**, 17–24.
64 K. Cooper, A. Gupta and S. Beaudoin, *J. Colloid Interface Sci.*, 2000, **228**, 213–219.
65 K. Cooper, N. Ohler, A. Gupta and S. Beaudoin, *J. Colloid Interface Sci.*, 2000, **222**, 63–74.
66 L. Wu, H. Feng, D. M. Guo and B. Zheng, *RSC Adv.*, 2014, **4**, 60002–60006.

